
Initial Target Experiments on the Upgraded OMEGA Laser System

A major program to demonstrate the feasibility of direct-drive laser fusion is underway at LLE. The overall goal of this program is to develop an understanding of target physics at the 30-kJ level that will allow the performance of direct-drive capsules designed for use with the National Ignition Facility (NIF) at the 1- to 2-MJ level to be predicted with confidence. The majority of the experiments that will contribute to this goal will be performed with the 60 UV (351-nm) beams of the recently upgraded, 30-kJ OMEGA laser system. The key physics issues that will be examined, both experimentally and theoretically, include irradiation uniformity, laser energy coupling and transport, laser-plasma interaction physics, hydrodynamic stability, and hot-spot and main-fuel-layer physics.

In this article we summarize initial target experiments performed with the upgraded OMEGA laser system.¹ Targets consisted mainly of glass microballoons (GMB's) having high initial aspect ratios ($R/\Delta R$, where R is the target radius and ΔR is the shell thickness) of ~ 150 to 300 , filled with either pure deuterium or an equimolar mixture of deuterium and tritium at pressures ranging from 5 to 20 atm. These low-mass shells were accelerated to high implosion velocities. The compressed fuel was predicted to have a high electron temperature (up to 6 keV) and a density in the range of 0.2 to 2 g/cm³. Diagnosis of target performance during the acceleration phase of the implosion was obtained from time- and space-resolved measurements of the x-ray emission from the laser-heated glass shells. Overall target performance was diagnosed by nuclear and particle instrumentation, from which estimates of the total thermonuclear yield and the fuel ion temperature were obtained. Neutron yields have been measured to be as high as 10^{14} (DT) and 1.1×10^{12} (DD), and ion temperatures up to 13 keV have been inferred from a neutron time-of-flight detector. High fuel electron temperatures of 3 to 4 keV have been inferred from spectroscopic measurements.

The main objective of these initial experiments was the activation of several key diagnostic systems. An x-ray framing camera and a Kirkpatrick-Baez (KB) microscope were used to

image the x-ray emission during the implosions. Copper and indium neutron activation counters were used to determine DT and DD neutron yields, and scintillator-photomultipliers were used to measure the neutron time-of-flight. Finally, a crystal spectrometer was fielded to measure the electron temperature from the continuum slope of the x-ray spectrum and from krypton K-shell spectroscopy.

X-Ray Imaging

1. X-Ray Framing Camera

A series of experimental shots were devoted to the initial activation of one of the x-ray framing cameras. The camera is based on the high-speed gating of a 0.25-mm-thick micro-channel plate with a channel-pore aspect ratio (length:diameter) of 40:1. The design and testing of the prototype for this camera are described in Ref. 2. The temporal resolution of the camera over a range of operating parameters was measured off-line using a short-pulse (300-fs) frequency-quintupled glass laser system. For the GMB's in this experimental series the camera was operated with an expected temporal resolution (gating time) of 35 to 40 ps.

Figure 64.1 shows a series of images recorded from shot 5067, sensitive to x rays in the spectral range above 3 keV. The target was a 20-atm DD-filled glass microballoon with an initial wall thickness of 2.3 μm and a diameter of 845 μm . The magnification was 6 \times and the calculated spatial resolution was $\sim 10 \mu\text{m}$ in the target plane. The time delay between strips is 250 ps, and the delay between images on a given strip is 50 ps. The fogging around the images in the third and fourth strips is caused by high-energy x rays produced during the implosion and transmitted through the 50- μm Ta pinhole substrate. The vignetting seen in the four corner images is caused by a circular aperture in the pinhole mount. The x-ray emission comes primarily from overdense glass plasma with an electron temperature ≥ 800 eV. During much of the implosion, before the glass has expanded significantly beyond its initial thickness, the location of the peak x-ray emission thus provides a good indication of the shell's location.

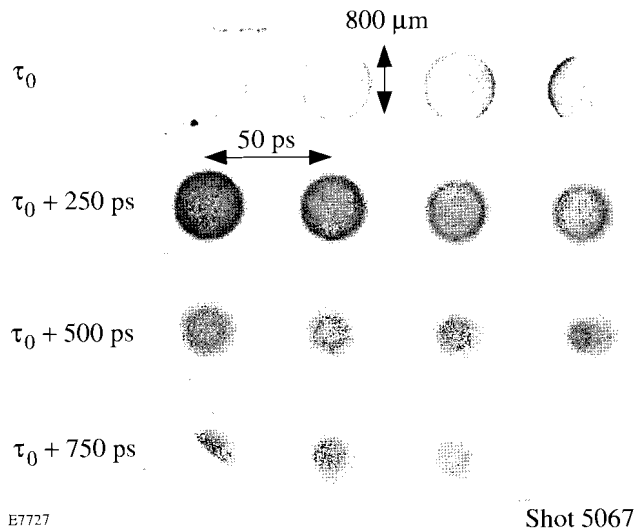


Figure 64.1

Framing-camera images of OMEGA shot 5067. The target was a glass microballoon with an initial wall thickness of $2.3 \mu\text{m}$ and a diameter of $845 \mu\text{m}$. The time delay between strips is 250 ps , and the delay between images on a given strip is 50 ps , time increasing from left to right. The magnification is $6\times$ and the calculated spatial resolution is $\sim 10 \mu\text{m}$.

To obtain a more quantitative understanding of the framing-camera images, the azimuthally averaged radius of the peak emission contour for each frame of Fig. 64.1 has been plotted in Fig. 64.2 as a function of time. Predictions based on the one-dimensional code *LILAC* are also plotted. *LILAC* uses a straight-line radiation transport algorithm to replicate the images, with spatial smearing based on the resolution of the pinhole. The temporal response of the diagnostic is modeled as being Gaussian in shape, with a 40-ps FWHM. Since no absolute timing fiducial is currently available for the camera, the zero time reference between the two data sets was taken as being the one that gave the best fit between the two. The time τ_0 of the first frame of Fig. 64.1 is then -200 ps , where $\tau = 0$ corresponds to the peak of the laser pulse. As can be seen, the predictions for the hydrodynamic motion of the shell are in good agreement with the experiment throughout the acceleration phase of the implosion ($\tau \approx 200 \text{ ps}$). However, during the subsequent coast phase of the implosion and at the onset of stagnation, the experiment deviates from the *LILAC* prediction. Emission from the glass comes from smaller radii than predicted, with the radius of peak emission continuing to decrease linearly with time until its stagnation at $\sim 350 \text{ ps}$. This departure from one-dimensional predictions may be due to the present level of laser-beam uniformity, in which case better results can be expected when beam smoothing is employed on the system. The successful deployment of this first x-ray

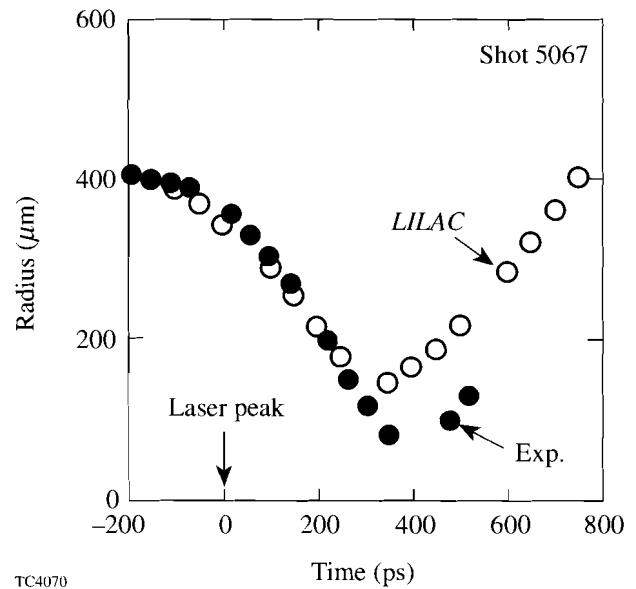


Figure 64.2

Radius of the peak x-ray emission contour for the target of Fig. 64.1 as a function of time. The solid circles are azimuthal averages obtained from the framing-camera images of Fig. 64.1, and the open circles are predictions of the one-dimensional code *LILAC*.

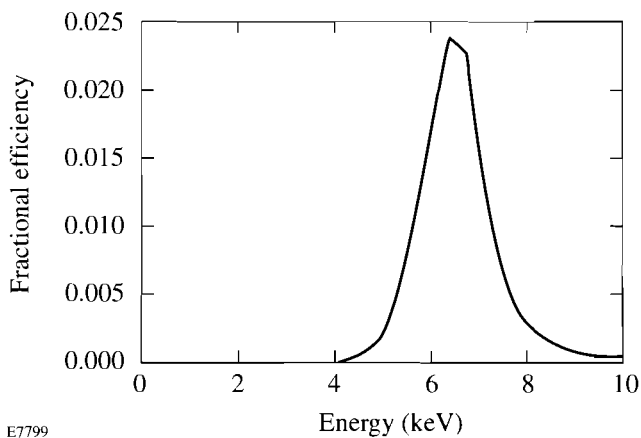
framing camera and the data obtained from it will allow improvements in target drive to be assessed when beam-smoothing techniques are implemented.

2. Kirkpatrick-Baez Microscope

A Kirkpatrick-Baez (KB) microscope—one of a set of new microscopes that incorporate improvements over the design used previously at LLE³—has been used to obtain time-integrated x-ray images of the initial target implosions. The reflective optics are Ir coated, extending their useful band up to 8 keV , while the resolution at the center of the field of view is $\sim 5 \mu\text{m}$.⁴ The KB microscopes thereby provide high-resolution, relatively hard x-ray images of target emission. They have been designed with precision pointing and focusing and are being fully calibrated in the x-ray laboratory at LLE. Eventually, the microscopes will be used for space-resolved continuum spectroscopy of implosions by incorporating a diffraction grating,⁵ and for framed monochromatic imaging by attaching a crystal monochromator and a framing camera assembly.⁴ The monochromator/framing camera attachment is being built by the laser fusion group at the Los Alamos National Laboratory.⁶

For the initial implosion experiments on OMEGA, a single KB microscope was deployed on the target chamber with a

simple arrangement of thin metallic filters. X-ray film (Kodak DEF) was used to record the images. Four images were obtained per shot through various filters. Since the targets used in these experiments were principally glass microballoons filled with either DD or DT, and since the glass contained a significant amount of a high-Z element (1%–2% RbO_2 molar), the shell emitted copious levels of relatively hard x rays (>4 keV). It was therefore necessary to filter the flux from the targets to limit the film exposure. Figure 64.3 shows the calculated response of the KB microscope versus energy for the Ir-coated mirrors and for a filtration of $203.2 \mu\text{m}$ of Be in combination with $101.6 \mu\text{m}$ of Al. The effective energy band is from 5 to 8 keV.



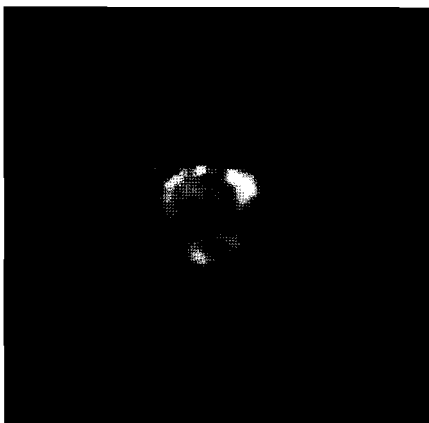
E7799

Figure 64.3
Calculated response of the KB microscope versus energy for 0.70° Ir-coated mirrors with a filtration of $203.2 \mu\text{m}$ of Be in combination with $101.6 \mu\text{m}$ of Al.

Figure 64.4 shows a comparison of pinhole camera and KB microscope images obtained on shot 5039. The target was a DT-filled glass microballoon overcoated with a $2\text{-}\mu\text{m}$ layer of CH. The increased resolution evident in the KB microscope image illustrates the benefit of the higher resolution and increased sensitivity of the KB microscope. The x-ray pinhole camera and the KB microscope were positioned within 10° of each other on the target chamber, minimizing differences due to view direction. They were similarly filtered so as to be sensitive to x rays of $>5\text{-keV}$ energy. The pinhole size was $10 \mu\text{m}$ and the magnification was 4.0. The microscope was operated at a magnification of 12.9. Both images were recorded on Kodak DEF film. One benefit of the increased sensitivity of the microscope is the ability to operate at higher magnifications, thereby reducing film grain noise as a contribution to image blurring. Clearly the increased spatial resolution allows for the imaging of finer details in the stagnation core.

For purposes of comparison with the previously described framing-camera results, Fig. 64.5(a) shows an image from shot 5067. The stagnation core can again be seen in this image. In this shot, as with many others not shown here, the right-hand side of the shell is much brighter than the left-hand side. A significant part of this effect is due to a systematic focus offset of the beams illuminating the left side of the target, a problem that has since been corrected. Using an intensity-converted horizontal lineout through the image [shown in Fig. 64.5(b)], the diameter of the stagnated shell can be estimated to be $192 \mu\text{m}$, based on the locations of peak emission on either side of the center. (The intensity conversions were accomplished using the semi-empirical formulas of Henke *et al.*⁷ and assuming an energy of 6 keV for the optical densities measured

(a) Pinhole camera image



(b) KB microscope image

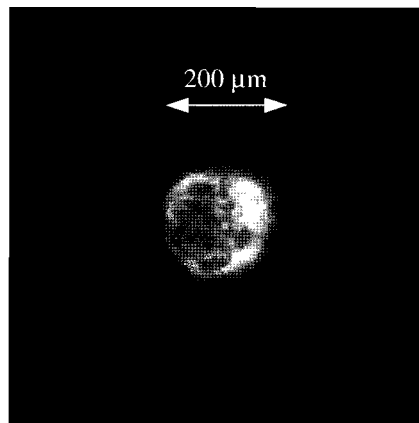


Figure 64.4

(a) Pinhole camera image and (b) KB microscope image of a 20-atm DT-filled glass microballoon of $840\text{-}\mu\text{m}$ diameter and $2\text{-}\mu\text{m}$ wall thickness, coated with $2 \mu\text{m}$ of CH (shot 5039). The two images have the same spatial scale and are viewed from within 10° of the same direction. The increased spatial resolution of the KB microscope is evident.

E7740

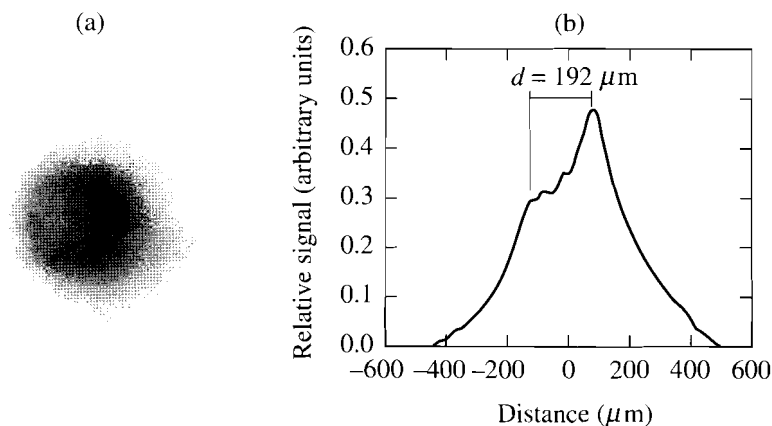
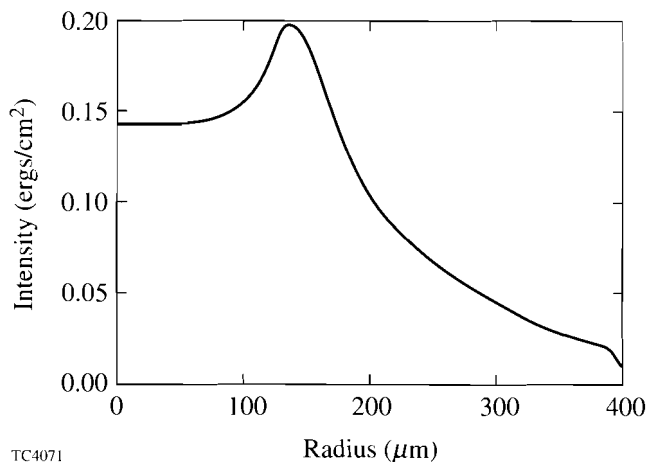


Figure 64.5

(a) KB microscope image of OMEGA shot 5067. The reflective optics are Ir coated, extending their useful band up to 8 keV, while the resolution at the center of the field of view is $\sim 5 \mu\text{m}$. (b) An intensity-converted horizontal lineout of the image in (a). The diameter of the stagnated shell is estimated to be $\sim 192 \mu\text{m}$.

E7800

in the DEF-recorded image.) *LILAC* predictions (Fig. 64.6) indicate a somewhat larger stagnated shell diameter of $275 \mu\text{m}$. This disagreement is consistent with what was seen with the framing-camera data above.



TC4071

Figure 64.6

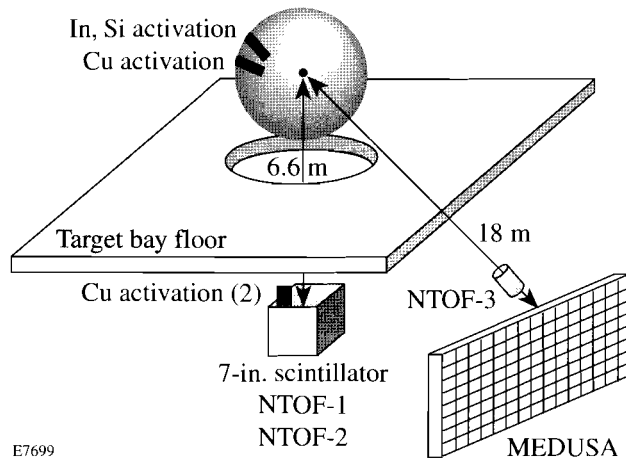
LILAC simulation of Fig. 64.5(b). The diameter of the stagnated shell, based on the location of peak emission, is predicted to be $\sim 275 \mu\text{m}$.

Fusion Experiments

A set of diagnostics that provided measurements of the neutron yield and the fuel ion temperature was used for these initial experiments. The neutron yield was measured by activation methods and scintillator-photomultiplier systems. Ion temperatures were measured using current-mode, quenched-scintillator/fast-photomultiplier detectors, with signals recorded by wide-bandwidth transient digitizers. Several detectors for both yield and ion temperature were used for each experiment.

The activation systems include copper and sodium activation for the detection of 14.1-MeV neutrons produced by DT fuel mixtures, and indium activation for the measurement of 2.45-MeV neutrons produced by pure deuterium fuel. The activation systems have been calibrated by the associated particle technique in a collaborative effort with the State University of New York at Geneseo. Two of the activation samples are inserted near the target (copper sample at 40 cm, indium sample at 25 cm) by a pneumatically operated rapid extractor. This system automatically transports the sample to the counting area, allowing rapid measurement while reducing the radiation exposure of personnel. On high-yield DT fuel target shots, the copper activation sample is placed 6.6 m from the target chamber in a holder near the other diagnostics (see Fig. 64.7). The sodium activation system uses self-activation/self-detection of sodium in a sodium-iodide gamma-ray detector crystal, which is located 6.6 m from the target chamber.⁸

A scintillator-photomultiplier system is also used to measure yield. This instrument consists of several large scintillators mounted at 6.6 m from the target and used as neutron time-of-flight spectrometers. These “yield” scintillators have active volumes of 2,500 and 44,000 cm^3 . The primary purpose of these devices is to allow the measurement of low primary and secondary yields. In the present high-yield experiments, the gain of the photomultipliers was reduced to prevent saturation. The data-acquisition subsystem consists of both transient recorders and, optionally, gated charge integrators. The charge integrators are gated to record individually the 2.45-MeV and the 14.1-MeV neutron signals for each detector. The scintillator yield measurements are calibrated *in situ* by comparison with the activation systems for both 2.45-MeV and 14.1-MeV neutrons.



E7699

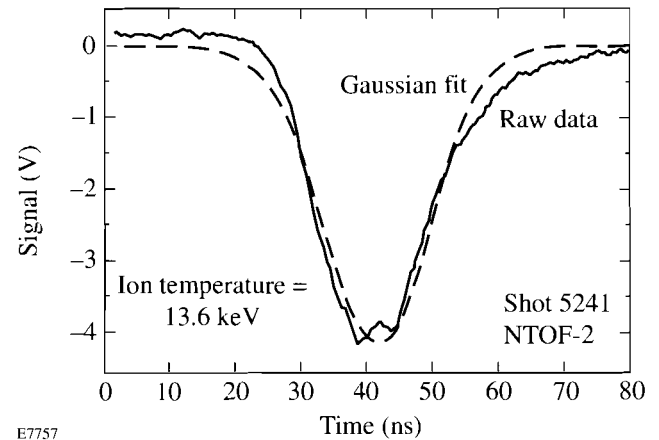
Figure 64.7
Schematic of the target chamber and the location of some of the neutron diagnostic systems.

Time-of-flight spectroscopy, using a GHz-bandwidth scintillator-photomultiplier-digitizer, currently provides ion-temperature measurements with low-temperature thresholds of 3.5 keV (for 14.1-MeV neutrons) and 0.2 keV (for 2.45-MeV neutrons). These detectors, along with the other scintillation detectors, are housed 6.6 m beneath the target chamber in a bunker with 20-cm-thick concrete walls and a 6-cm-thick lead faceplate to reduce the effects of prompt n - γ radiation (see Fig. 64.7). An additional fast time-of-flight detector is being installed in the neutron diagnostic room at a distance of 18 m from the target chamber; this will provide the higher resolution required for low-temperature DT implosion experiments.

A series of experimental shots were designed to provide a wide range of DT and DD yields to aid in the calibration of the activation counters and scintillators. Table 64.I presents typical neutron data from five target shots. The system response

(including the scintillator, photomultiplier, coaxial cable, and recording digitizer) for neutron time-of-flight measurements was determined by applying a short (100-ps) light pulse to the detector package. This system response was deconvolved from the raw experimental signal (an example of which is shown in Fig. 64.8) to obtain the neutron-averaged ion temperatures quoted in Table 64.I. The one-dimensional *LILAC* predictions for yield, neutron-averaged ion temperature, and convergence ratio are also included in Table 64.I. The five shots corresponded to a wide range of targets. Shot 5241, which gave the highest ion temperature, used a thin (2.7- μm) bare glass shell, while the other shots included plastic shells (shots 5212 and 5221) and plastic-coated glass shells (shots 5049 and 5276).

After the calibration series of shots, emphasis was placed on maximizing the yield in both DT and DD implosion experiments. The design of these experiments focused mainly on



E7757

Figure 64.8
Signal obtained from a scintillator-photomultiplier neutron time-of-flight detector placed at 6.6 m from the target. The Gaussian fit to the raw data corresponds to an ion temperature of 13.6 keV.

Table 64.I: Summary of neutron yields and ion temperatures.

Shot Number	Fuel	Neutron Yield		Ion Temperature (keV)		Calculated Convergence Ratio
		Measured	Calculated	Measured	Calculated	
5049	DT	1.0×10^{14}	2.0×10^{14}	—	15.0	4.4
5212	DD	5.9×10^{10}	1.7×10^{11}	4.7	2.3	19.3
5221	DD	4.8×10^{10}	1.6×10^{11}	6.1	2.4	19.0
5241	DD	5.7×10^{11}	9.3×10^{11}	13.6	17.0	5.2
5276	DT	4.9×10^{13}	1.7×10^{14}	7.8	9.3	8.6

reducing the calculated convergence ratio of the pellet during the implosion. The calculated convergence ratio is defined as the ratio of the initial fuel-pusher interface radius to the calculated radius of this same interface at stagnation. It is well established on the basis of stability considerations that one is able to obtain an increasing fraction of the one-dimensionally calculated neutron yield as the calculated convergence ratio is decreased.^{9,10} With the limited set of targets available, several options were investigated to reduce the calculated convergence ratio of the implosions while maximizing the one-dimensional yield. A solution was found in overcoating the bare glass microballoons with several microns of parylene and then targeting OMEGA at tighter-than-normal focusing.

Results for the DT neutron yield as a function of UV energy on target are shown in Fig. 64.9. The maximum yield (1.0×10^{14}) is the highest recorded to date from any laser system. It must again be noted that precision energy balance, power balance, and beam smoothing have not yet been implemented on OMEGA. Consistent with the discussion of the x-ray images above, the symmetry of the implosions may well have suffered from high initial levels of on-target irradiation nonuniformity. For the shot producing 10^{14} neutrons, the calculated convergence ratio was 4.4 and the yield was a fraction 0.52 of the one-dimensional yield. The fusion energy released from this shot was equal to 1% of the laser energy delivered to the target (1% of scientific breakeven).

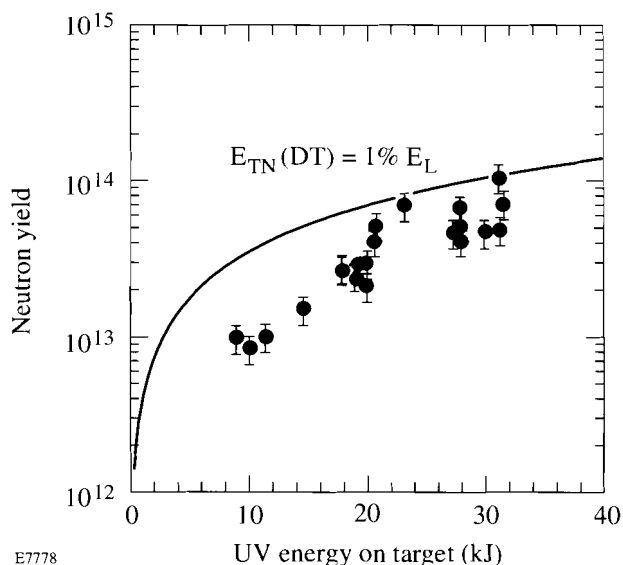


Figure 64.9

Performance summary of initial high-yield implosion experiments. The solid curve indicates the neutron yield corresponding to a fusion energy release equal to 1% of the UV energy on target (1% of scientific breakeven).

X-Ray Spectroscopy

It was predicted that high electron temperatures up to 5 keV could be achieved on OMEGA by using relatively thin shell targets. These temperatures would occur at modest compressed densities (~ 1 to 5 g/cm^3), and the ion temperatures would peak at above 10 keV at the center of the compressed core. New diagnostic techniques were thus developed for measuring these temperatures, using K-shell line and continuum spectroscopy of krypton-doped targets.^{11,12} (See also the next article in this issue.) A series of krypton-doped, deuterium-filled targets were shot on OMEGA to test these predictions. A strong K-shell Kr spectrum was indeed observed, and high electron temperatures were determined, in close agreement with code predictions. These targets were similar to those of Table 64.I for which high ion temperatures were measured.

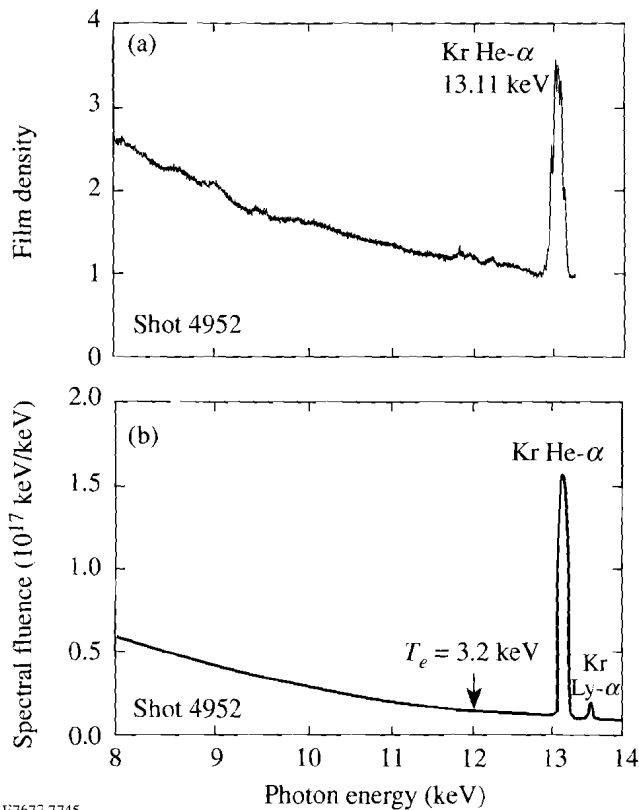
The krypton lines observed in these shots have the highest energies, 13 to 16 keV, that have been observed in laser-fusion experiments. Previously, only the Kr^{+34} resonance line (at 13.1 keV) had been observed, using a Von-Hamos focusing spectrometer on the 24-beam OMEGA system operating in short-pulse mode (100 ps, 6 TW).¹³

Results from the present experiments are shown from two Kr-doped target shots for which the experimental parameters are listed in Table 64.II. In the first shot, a Si(111) diffracting crystal was used, tuned to detect the spectral range of 8 to 13 keV, while in the second shot a LiF(200) crystal was used, tuned to the range of 12 to 20 keV.

Figure 64.10 shows a comparison between the measured and simulated spectra from shot 4952. In Fig. 64.10(a), the raw experimental spectrum is shown in film density units. In Fig. 64.10(b), a time- and space-integrated *LILAC* simulation of the same spectrum is shown. This simulation was carried out using a non-LTE radiation transport postprocessor that includes a time-dependent multispecies ionization and level-population model based on a simple screened-hydrogenic description of the principal atomic states. Figure 64.11 shows a similar comparison between experiment and simulation for shot 5110. In both cases the simulated spectrum is plotted on a linear scale, in line with the fact that film density and exposure are approximately linear for the photon energy range detected (see below). The He- α line in Fig. 64.11 has a film density higher than 5 and saturates the film. Instrumental broadening of the lines has been included in the simulation. In comparing the measured and simulated spectra, it should be noted that *LILAC* does not calculate the satellite lines on the low-energy side of the He- α and He- β lines, nor the lines above

Table 64.II: Experimental parameters of two CH target shots analyzed using krypton line and continuum spectroscopy.

Shot No.	Target diameter (μm)	Target thickness (μm)	DD pressure (atm)	Krypton pressure (atm)	Laser energy (kJ)
4952	870	10.0	10	0.03	23.6
5110	874	12.4	10	0.03	29.5



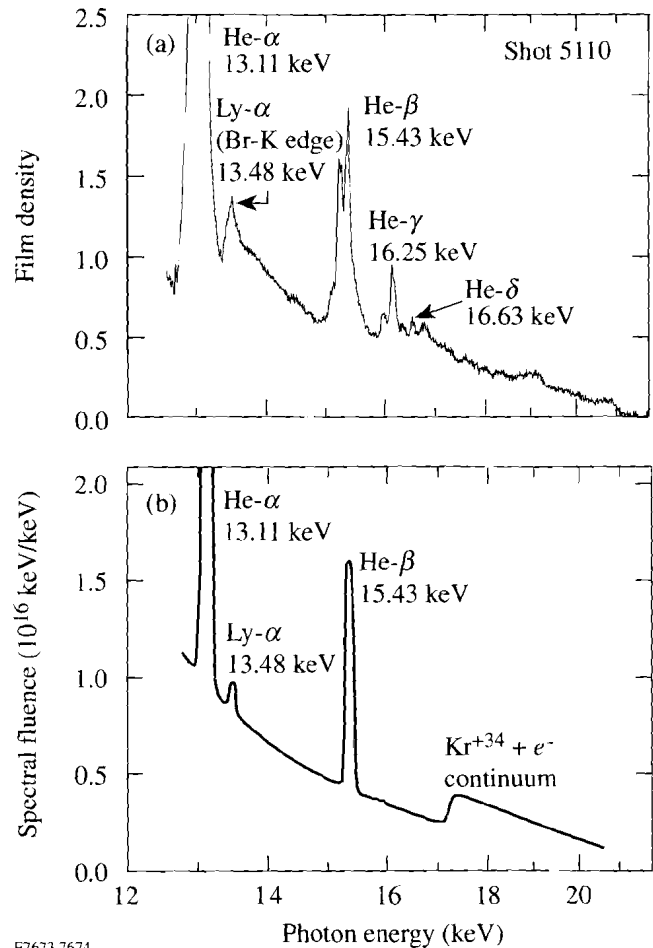
E7677.7745

Figure 64.10

(a) Experimental spectrum from Kr-doped, DD-filled target shot 4952. (b) *LILAC* simulation of the same spectrum. The continuum slope around 12 keV in (b) implies $T_e = 3.2$ keV. Instrumental broadening of the calculated lines has been included. The simulation does not include the satellite lines on the low-energy side of the He- α line.

16 keV. Also, accounting for film and crystal calibration increases the experimental high-energy continuum and brings it into closer agreement with the simulated one.

To analyze the spectra quantitatively, the responses of the film (Kodak DEF) and the crystals (LiF and Si) have to be known. Henke¹⁴ published a model for the response of DEF film and normalized it to experimental values below 10 keV. Using this model and updated x-ray absorption coefficients in



E7673.7674

Figure 64.11

(a) Experimental spectrum from Kr-doped, DD-filled target shot 5110. The He- α line has a film density >5 and saturates the film. (b) *LILAC* simulation of the same spectrum. The simulation does not include the satellite lines on the low-energy side of the He- β line or the lines above 16 keV. Instrumental broadening of the calculated lines has been included.

the film constituents, we calculated the film response for photon energies below and above 10 keV. Figure 64.12 shows the results in the 1- to 30-keV range, for various film density values between $D = 0.5$ and $D = 3$ (in increments of 0.5), assuming that the film density was measured with a numerical

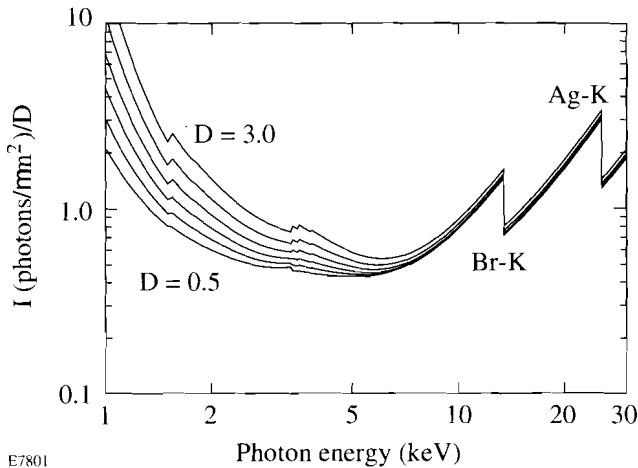


Figure 64.12

Calculated DEF film response for various film-density values between $D = 0.5$ and $D = 3$ (in increments of 0.5), assuming that the film density was measured with a numerical aperture of 0.25. Jumps in response due to the K edges of Br and Ag are marked. Henke's model was used, with updated coefficients for x-ray absorption in the film constituents.

aperture of 0.25. Jumps in film response due to the K edges of Br and Ag are marked. Figure 64.12 shows that for film densities below $D \sim 2$ and photon energies above ~ 6 keV, the film density is proportional to exposure. This is the reason for plotting the spectral fluence in Figs. 64.10 and 64.11 on a linear scale.

For the Si(111) crystal, published diffraction data¹⁵ were used. For the LiF(200) crystal, published calibration data¹⁶ were used as well, and they agree with previous data for LiF(200) crystals used at LLE.¹⁷ It should be emphasized that for the purpose of temperature determination only the changes with photon energy of the film and crystal responses are required. Using the film exposure $I(\text{keV}/\text{cm}^2)$ and the integrated crystal reflectivity R , the spectral fluence per unit solid angle of the target can be determined. For example, the resulting continuum fluence at a photon energy $E(\text{keV})$ is given by $S(\text{keV}/\text{keV}) = I(E)L^2 \tan \theta_B / (RE \cos \alpha)$, where L is the target-film distance (along the ray), θ_B is the Bragg angle, and α is the angle of incidence on the film.

Using the film and crystal calibrations as described above, the spectral data were converted to spectral fluence in absolute units. The continuum slopes in the ranges 8 to 13 keV for Fig. 64.10 (shot 4952) and 16.5 to 20.5 keV for Fig. 64.11 (shot 5110) were used to estimate the electron temperature by fitting exponential curves. Figure 64.13 shows the result for shot

4952 where fitting to the high-energy part of the continuum yields a temperature of 3.1 keV. For shot 5110, the measured temperature was 4.0 keV. The simulated spectra show, in agreement with the experiment, that higher-energy portions of the continuum yield higher temperatures. This is because these portions are preferentially emitted at the higher-temperature regions (and times). The experimental result for shot 4952 agrees with the simulated temperature of 3.2 keV, obtained from the slope of the simulated spectrum in the same spectral range. The absolute magnitude of the continuum is lower than that of the simulated spectrum by only about a factor of 1.5; comparison of the absolute magnitude of spectral lines is complicated by such factors as detailed atomic physics modeling and the spatial distribution of the emitting source.

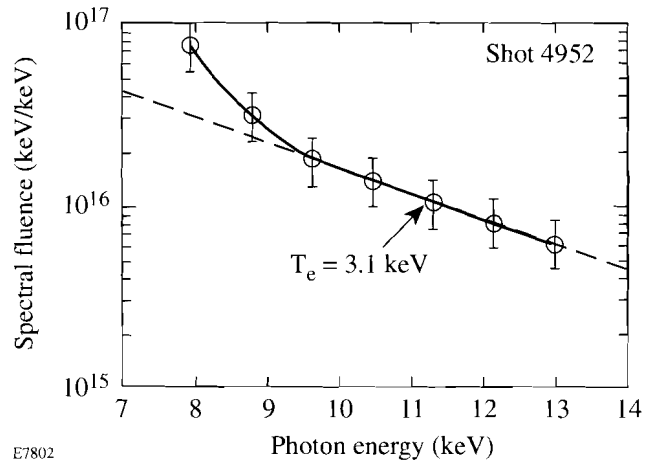


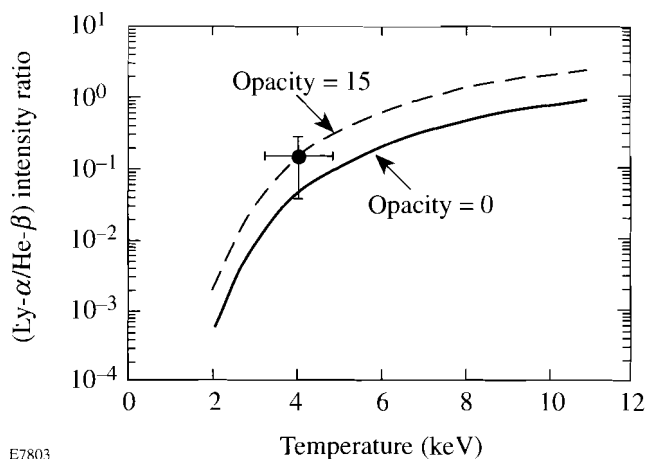
Figure 64.13

Experimental continuum spectrum of Fig. 64.10(a) after absolute calibration. The slope in the 10- to 13-keV range indicates an electron temperature of $T_e = 3.1$ keV.

LILAC results show that the space-averaged temperatures around peak compression in these shots were 3 to 4 keV and the maximum temperatures were 5 to 6 keV. The ion temperatures in such thin-shell implosions are predicted to be significantly higher than the electron temperatures, consistent with the experimental results reported in Table 64.I.

An additional method for estimating the electron temperature involves the measured intensity ratio of the Lyman- α line of Kr^{+35} to the helium- β line of Kr^{+34} . As described in Ref. 11, this ratio is highly sensitive to the temperature below ~ 8 keV and changes very little with density. Also, the spectral lines chosen can have a relatively low opacity (unlike that of the He- α line); this is true for the krypton fill pressure and compression in these experiments. However, it was shown¹⁸

that a high opacity of the He- α line can indirectly increase the Lyman- α to helium- β ratio for the same temperature; this is because the He- α opacity facilitates ionization of the helium-like state through $n = 2$ excited Kr⁺³⁴ ions. Figure 64.14 shows curves of the calculated intensity ratio¹² of these two lines, with and without a correction for the opacity of the He- α line. The curve used here for the temperature determination corresponds to the opacity ($\tau = 15$) for shot 5110, estimated on the basis of LILAC-predicted profiles. A complication arises because the wavelength of the K edge of Br (in the film grains) practically coincides with that of the Lyman- α line of Kr⁺³⁵, giving rise to a jump in the film response at that wavelength. The corresponding jump in the measured spectrum should be smaller than what is indicated in Fig. 64.12 because of the finite spectral resolution of the spectrometer (which blends the intensity around the jump). To account approximately for this effect, the continuum at energies above the K edge was extrapolated toward lower energies and the resulting jump in the continuum was subtracted from the measured peak at 13.5 keV. The resulting estimated temperature (see Fig. 64.14) is 4.1 keV.



E7803

Figure 64.14

Electron-temperature determination by the measured intensity ratio of the Lyman- α to helium- β lines. The curves of calculated intensity ratio are taken from Ref. 12. This ratio depends weakly on the density, but it does depend significantly on the opacity of the He- α line. The curve used here for the temperature determination corresponds to the estimated opacity ($\tau = 15$) for shot 5110.

In the future, the ion temperature in similar experiments will be measured through the Doppler broadening of Kr lines, using a recently completed focusing x-ray spectrograph of high spectral resolution. Finally, the measurements will be extended to include L-shell Kr lines. It is shown in the following article that the simultaneous measurement of K- and

L-shell lines can be used to determine the fuel ρR and to study core-shell mixing.

Summary

Initial target experiments have been performed with the upgraded OMEGA laser, using glass and CH microballoons filled with either pure deuterium or DT. During these experiments several key diagnostic systems have been activated including an x-ray framing camera, a Kirkpatrick-Baez (KB) microscope, copper and indium neutron activation counters, scintillator-photomultipliers, and a crystal spectrometer. The framing camera has been used to diagnose the target implosion dynamics, which agree well with predictions up to the stagnation phase. Deviations from predictions, also seen using the KB microscope, are consistent with the present lack of beam smoothing on the laser. Neutron yields up to 10^{14} (1% of scientific breakeven)—the highest recorded to date from any laser system—have been obtained from DT targets and fuel ion temperatures up to 13 keV have been measured. Spectroscopic diagnostics based on the continuum slope and krypton line ratios have demonstrated electron temperatures from 3 to 4.1 keV. Taken as a whole, these results demonstrate a successful integration of laser operations and target diagnostics into the OMEGA experimental system.

ACKNOWLEDGMENT

This work was supported by the U.S. Department of Energy Office of Inertial Confinement Fusion under Cooperative Agreement No. DE-FC03-92SF19460, the University of Rochester, and the New York State Energy Research and Development Authority. The support of DOE does not constitute an endorsement by DOE of the views expressed in this article.

REFERENCES

1. Laboratory for Laser Energetics LLE Review **63**, NTIS document No. DOE/SF/19460-91, 1995 (unpublished), p. 99.
2. D. K. Bradley, P. M. Bell, O. L. Landen, J. D. Kilkenny, and J. Oertel, *Rev. Sci. Instrum.* **66**, 716 (1995).
3. Laboratory for Laser Energetics LLE Review **46**, NTIS document No. DOE/DP/40200-156, 1991 (unpublished), p. 91.
4. F. J. Marshall and Q. Su, *Rev. Sci. Instrum.* **66**, 725 (1995).
5. F. J. Marshall, J. A. Delettrez, R. Epstein, and B. Yaakobi, *Phys. Rev. E* **49**, 4381 (1994).
6. J. A. Oertel, T. Archuleta, L. Clark, S. Evans, A. Hauer, F. J. Marshall, C. G. Peterson, T. Sedillo, C. Thorn, and R. G. Watt, in *Ultra-high- and High-Speed Photography, Videography, and Photonics '95*, edited by D. R. Snyder and G. A. Kyrala (SPIE, Bellingham, WA, 1995), Vol. 2549, p. 82.

7. B. L. Henke, E. M. Gullikson, and J. C. Davis, *At. Data Nucl. Data Tables* **54**, 181 (1993).
8. R. A. Lerche, Lawrence Livermore National Laboratory Laser Program Annual Report 1978, UCRL-50021-78 (1979), p. 6-53.
9. Laboratory for Laser Energetics LLE Review **28**, NTIS document No. DOE/DP/40200-26, 1986 (unpublished), p. 159.
10. Laboratory for Laser Energetics LLE Review **40**, NTIS document No. DOE/DP/40200-102, 1989 (unpublished), p. 171.
11. Laboratory for Laser Energetics LLE Review **61**, NTIS document No. DOE/SF/19460-58, 1994 (unpublished), p. 1.
12. B. Yaakobi, R. Epstein, C. F. Hooper, D. A. Haynes, and Q. Su, submitted for publication to the *Journal of X-Ray Science and Technology*.
13. B. Yaakobi and A. J. Burek, *IEEE J. Quantum Electron.* **QE-19**, 1841 (1983).
14. B. L. Henke *et al.*, *J. Opt. Soc. Am. B* **3**, 1540 (1986).
15. G. Brogren and E. Lindén, *Ark. Fys.* **22**, 535 (1962).
16. D. B. Brown and M. Fatemi, *J. Appl. Phys.* **45**, 1544 (1974).
17. A. J. Burek and B. Yaakobi, Final Report to the National Bureau of Standards contract NB81NAHA2032 (1983), Appendix A.
18. C. J. Keane *et al.*, *Phys. Fluids B* **5**, 3328 (1993).